CIRP Annals - Manufacturing Technology 00 (2025) 1–5

Contents lists available at ScienceDirect

CIRP Annals - Manufacturing Technology

journal homepage: https://www.editorialmanager.com/CIRP/default.aspx

Towards large-scale production of improved magnetic flux guidance structures in non-grain-oriented electrical steel

Phillip Stöcks-Morgan[a], Tobias Neuwirth[b], Achref Douiri[c], Simon R. Sebold[b], Anders Kaestner[d], Christoph Hartmann[a], Nora Leuning[c], Michael Schulz[b], Wolfram Volk (1)[a,*]

[a] Chair of Metal Forming and Casting, Technical University of Munich, Walther-Meissner-Str. 4, 85748 Garching, Germany
[b] Heinz Maier-Leibnitz Zentrum (MLZ), Technical University of Munich (TUM), Lichtenbergstr. 1, Garching, 85748, Germany
[c] Institute of Electrical Machines, RWTH Aachen University, Schinkelstrasse 4, 52062 Aachen, Germany
[d] PSI Center for Neutron and Muon Sciences, Villigen, 5232, Switzerland

ARTICLE INFO

Article history:
Available online xxx

Keywords:
Residual stress
Electric vehicle
Press

ABSTRACT

Modern synchronous electric drives require magnetic anisotropy in their rotor, manufactured from non-oriented electrical steel. Conventionally, flux barriers are placed on electrical steel sheets by removing the material, creating small recesses. While the approach is magnetically effective, the rotor is mechanically weakened. Embossed flux barriers offer an approach to stiffen the rotor mechanically, increasing efficiency. The required micro-embossing was successfully produced on an industry-grade press for the first time. Magnetic characterisation of the samples using neutron grating interferometry and a single sheet tester shows that the novel technology is transferrable from the laboratory frame to large-scale industrial manufacturing processes.

1. Introduction

Modern electrical machines are mass-produced products and are a key component for making mobility more efficient and sustainable. Around 46% of global electricity demand is for motor-driven systems, whereas a third of that share is for mechanical movement [1]. Hence, even minor improvements in electrical motors lead to a substantial absolute efficiency gain. Thin laminations of non-grain-oriented (NO) electrical steel form the magnetic core of rotating electrical machines. These thin metal sheets are conventionally shear cut and then stacked (see Fig. 1a). For permanent magnet synchronous machines (PMSM), strong magnetic coupling of the rotor and stator and a high magnetic anisotropy are desired. Typically, anisotropies are manufactured through shear cut recesses acting as flux barriers [2]. Since these recesses weaken the rotor mechanically, micro-embossed flux barriers offer an alternative forming process for magnetic flux guidance, increasing mechanical strength [3]. This contribution explores the transferability of the approach from the laboratory-scale to large-scale manufacturing processes.

An electrical motor acts as an energy converter from electrical to mechanical energy, with different conversion losses, such as mechanical losses, copper losses (in the coils and copper conductors), and core losses (i.e. iron losses). These core losses are due to eddy currents and the hysteresis of the core material [4]. Pure iron offers the highest elementary saturation magnetization, a high relative permeability μ_R and low coercivity [5]. Adding up to 3% silicon to the iron increases the electrical resistivity ρ and μ_R [6]. Hence, NO-silicon steel allows for reduced eddy currents and a stronger magnetic coupling and is currently the material of choice for most rotating electrical machines [5,6].

The manufacturing process introduces anisotropies into NO electrical steel, such as rolling direction (RD) and production-induced mechanical and thermal stresses [7]. This impairs the magnetic properties of the material. Shear cutting introduces mechanical stress around the shear-cut-zone (SCZ) [8]. A weakening of the magnetic properties of electrical steel is observed around the SCZ [9]. The magnitude of the magnetic weakening of the material is influenced by the used cutting clearance (CCL) and the edge quality of the punch and die [10]. An increased edge length for a reference volume increases the effect [9]. Furthermore, the magnetic weakening of the material is frequency-dependent [11].

A high magnetic anisotropy in synchronous machines, i.e. steep permeability gradients in the rotor, is usually not achieved through

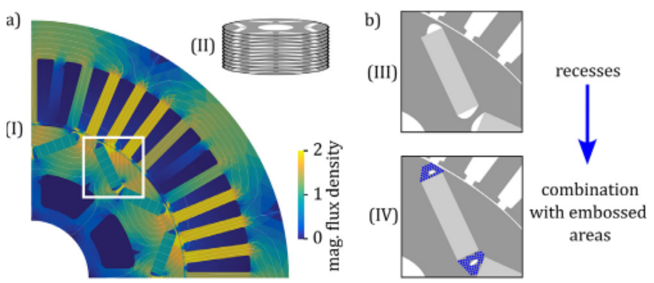

Fig. 1. a) Magnetic simulation of a PMSM-geometry with classical flux barriers (I) and stacked rotor sheets (II); b) magnified flux barriers: permanent magnets are depicted in light grey, electrical steel in dark grey showing classical recesses (white areas around the magnets) (III) and the novel combinatory approach (IV) with embossed flux barriers in blue.

* Corresponding author.
E-mail address: wolfram.volk@utg.de (W. Volk).

https://doi.org/10.1016/j.cirp.2025.03.021
0007-8506/© 2025 Published by Elsevier Ltd on behalf of CIRP.

the choice of the core material. Conventionally, the anisotropy is realised by placing recesses in the electrical steel rotor [2]. While the relative permeability μ_R of modern electrical steels is ~15,000, a relative permeability of air of ~1 can be assumed for the recesses [12]. Fig. 1a) visualises a magnetic simulation of a PMSM design, showing small recesses around the magnet fittings, acting as flux barriers.

Since the permanent magnets are placed relatively close to the stator, achieving a strong magnetic coupling of the rotor and stator requires the flux barriers between the poles of the magnets to be placed even closer to the edges of the rotor, leading to thin remaining bridges. When operating the motor, however, the torque and the centrifugal forces are then concentrated on these thin bridges, resulting in a mechanical limit for the maximum rotational speed. Since manufacturing-induced residual stress lowers the μ_R, the targeted application of residual stress to locally lower the permeability of the electrical steel offers an alternative approach to local magnetic flux guidance [3,13]. Pyramid-shaped micro-indents, in particular, are generally suitable for local magnetic flux guidance. The embossing is small enough to ensure the sheets can be easily stacked. Embossing on both sides facilitates this aim, leading to more symmetric flux barriers. With micro-embossing, local μ_R ~2000 can be reached [3,14] Since this is still some order of magnitude higher than classical recesses, a combinatory approach is most promising for improved rotor designs. This alternative approach allows for mechanically more stable rotor designs compared to classical recesses. A modified rotor geometry is illustrated in Fig. 1b).

This work presents neutron-based locally resolved magnetic measurements, suggesting that novel embossed flux barriers can be integrated into large-scale manufacturing processes. Micro-embossed flux barriers are produced on a large area (up to 30×30 mm^2) on both sides of the sheet metal simultaneously on an industry-grade press for the first time. Potential influences for transferring the approach from the laboratory scale to large-scale production are studied, i.e. transitioning embossing from the laboratory scale to an industry-grade press. Since rotor geometries are usually shear cut from electrical steel sheets [2], the interaction of embossed flux barriers and shear cut edges is studied; this includes the ideal process sequencing.

2. Setup

2.1. Material

All samples presented in this study were made from a NO fully processed electrical steel with 350 µm thickness and no insulation layer applied from board material. The silicon content of the material is 2.4 %wt, with a mean grain size of 55 µm. The material has a yield strength of 363 MPa, an ultimate tensile strength of 464 MPa, a uniform elongation of 17.7% and an elongation at fracture of 24.6% [10].

2.2. Sample production

Samples were produced at the Technical University of Munich from the material introduced in 2.1. Samples presented in 3.1. measure 60×30 mm^2 and 60×10 mm^2 for 3.2. and 3.3.; the external field (H_A) was applied, as shown in Fig. 2a). The shear cut samples for this study

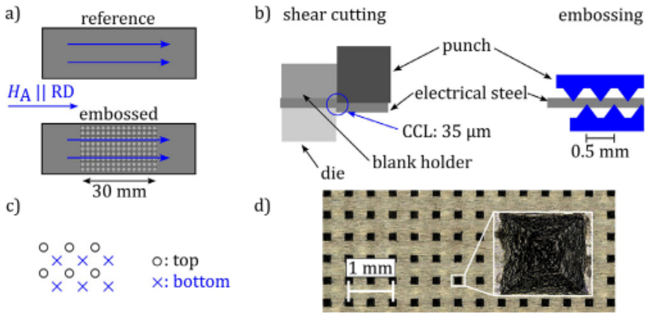

Fig. 2. a) Sample geometry, edges are shear cut or wire-cut; b) sample preparation; c) embossing geometry; d) image of an embossed specimen.

were produced with a high-precision punching tool. A fixed CCL of 35 µm with sharp edges on the punch and die was used. The punch and die were made from carbide containing 87 wt.% tungsten and 12 wt.% cobalt [10]. The tool was operated on a mechanical press at a 32 mm stroke. Embossed samples for this study were produced on a high-precision embossing tool. Embossing was realised simultaneously with pyramid-shaped indents from both sides, covering the full sample width and 30 mm length, see Fig 2a). The embossing punches are made from hardened 1.2379 tool steel. The upper embossing punch is shifted diagonally relative to the lower one to obtain a diagonally offset embossing pattern, see Fig. 2c). The embossing punches use a quadratic embossing pattern, with a distance of 0.5 mm between the embossing pyramids, see Fig 2d). This tool was operated on a universal testing machine and a press at 19 mm stroke. The embossing tool has a piezo-force sensor and a laser distance sensor. The embossing force per point F_{EB} was kept constant at 50 N and varied to 75 N and 100 N, as shown in 3.2. A Bruderer BSTA 50−110 eccentric press in single-stroke mode at 100 strokes per minute was used for industry-grade operation of the embossing and punch tools. Wire-cut EDM reference samples were manufactured externally. Laser-optical analysis was conducted on a Keyence VK-X100 Laser scanning microscope.

2.3. Local magnetic measurements: neutron grating interferometry

The local magnetization is mapped using the interaction of the magnetic moment of the neutron with the magnetic domain structure inside a ferromagnetic material. This interaction causes ultra-small-angle neutron scattering (USANS), which is recorded by neutron grating interferometry (nGI), an advanced non-destructive neutron imaging technique [15,16]. The spatially resolved USANS distribution is called the dark field image (DFI).

A change in the magnetic domain distribution results in a corresponding change in the DFI signal. An increase in magnetization increases the DFI signal while introducing residual stress leads to a decrease in the signal. The measurements were performed at the ICON neutron imaging beamline [17] located at PSI Center for Neutron and Muon Sciences using the nGI setup developed at Heinz Maier-Leibnitz Zentrum (MLZ) [14]. For the magnetization of the samples, a custom-built magnetic yoke with a maximum applied magnetic field of 1000 A/m was used.

2.4. Global magnetic characterisation

The metrological characterisation of the magnetic properties was performed on a 60×60 mm^2 single sheet tester (SST) at the Institute of Electrical Machines at RWTH Aachen University. The SST setup by Brockhaus Measurements incorporates two winding systems for high-frequency and low-frequency measurements with ratios of primary to secondary windings N_1/N_2 of 25/25 and 115/155, respectively. Magnetic polarisation J_{max} was sinusoidal, with the form factor error used as a quality criterion. The samples were characterised at frequencies of 50 Hz, 100 Hz, 200 Hz, 400 Hz, 700 Hz, and 1000 Hz and polarization of 0.1 T up to a maximum of 1.8 T in 0.1 T-steps. Within the scope of the presented study, the magnetization curve, i.e. magnetic polarisation as a function over the applied magnetic field $J_{max}(H_{max})$, respective iron losses P_s and relative permeability μ_r is evaluated.

3. Results and discussion

3.1. Transfer from test setup to industrial press

Previous studies produced embossed specimens with lab-scale single-embossing or, if simultaneously, on a universal testing machine [3,13]. The influence of transferring the approach to a high-speed eccentric blanking press is studied: This investigation assesses whether the transfer from the testing machine (TM) at slow speed to a high-speed eccentric press (EP) yields a similar embossing homogeneity for a large embossed area of 30×30 mm^2 on 60×30 mm^2 samples with wire-cut edges. The duration of force transmission to the sheet metal during embossing is 22.64 s for TM and 0.07 s for EP. The

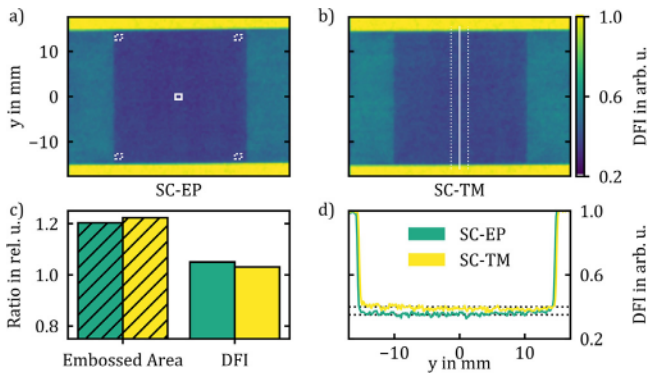

Fig. 3. Comparison of the difference in DFI signal for samples made using a) an eccentric press and b) a universal testing machine at 1000 A/m; c) homogeneity analysis edges/centre from regions marked in a) comparing base areas of the indents and the DFI signal; d) DFI signal profiles perpendicular to the magnetization direction, as marked in b).

total embossing force was set to 180 kN for both machines (3600 embossing points on one side); F_{EB} on the eccentric press deviated and was around 10% higher due to setup limitations on the EP.

DFI images of the samples at 1000 A/m are depicted in Fig. 3a) and in Fig. 3b), respectively. These maps show that both processes produce generally homogeneous areas of flux suppression. To highlight the homogeneity between the edge and central region, the deformed area (pyramid base area), determined with optical microscopy, and the DFI signal were compared. Fig. 3c) depicts the ratio when comparing four edge regions, marked in Fig. 3a) to a middle region for both samples. The geometrical homogeneity ratio for both samples deviates only 2%, and the EP yields slightly better homogeneity. The DFI ratios, however, show a reciprocal deviation of about 2%. This trend is to be expected since larger deformed areas would yield a steeper residual stress gradient, resulting in a lowered DFI signal. Overall, the magnetic DFI measurements show fewer homogeneity deviations from edges to centre than the geometrical measurements, positively affecting homogenous flux suppression. Furthermore, the TM and EP samples show similar geometrical and magnetic homogeneity, justifying the transfer from TM to EP. We note that the line profile perpendicular to the magnetization direction, presented in Fig. 3d), shows a slight decrease of the DFI signal towards the lower edge for the TM, while EP shows no such trend. This likely results from a slight misalignment of the punches during embossing. At the same time, the lower DFI signal in the EP indicates an increased flux suppression, which we attribute to the deviated F_{EB}.

3.2. Magnetic compatibility of cutting methods and embossing

To assess the integrability of embossed flux barriers in the shear cutting process of electrical steel sheets, wire-cut (E) and shear cut (SC) edges with embossed (EB) and not-embossed reference (R) areas are compared. All SST-studied EB samples were produced on the eccentric press. SST data is analysed for global magnetic characterisation. For a fixed frequency of f = 50 Hz, the relative permeability μ_r of all EB specimens is lower than the reference R specimen, as shown in Fig. 4a) as a function of J_{max}. The reference sample E-R achieves a maximum μ_r of 5887 at 0.6 T With F_{EB} = 50 N this value is reduced to 1384 at 0.3 T for E-EB, with further decreases observed at higher embossing forces of 75 N and 100 N, as shown in Fig. 4b). This shows that embossed flux barriers can be applied simultaneously on industrial presses, causing the expected deterioration in μ_r. The influence of the SCZ is visible when comparing the E-R and SC-R samples, where $\mu_{r,max}$ is lowered to 5238 at 0.6 T, 11 % lower than for E-R. The difference is, however, less pronounced when combined with embossing. SC-EB has with 1354 at 0.3 T only a 2% lower $\mu_{r,max}$ than E-EB. The data suggests that, when superimposed with embossing, the influence of the SCZ decreases.

This is validated with nGI measurements of E-R, SC-R, E-EB (50 N) and SC-EB (50 N) magnetized with 1000 A/m. The resulting DFI maps in Fig. 5a) show a reduced DFI signal in the SCZ of SC-R and SC-EB (50 N) and no reduction at the cut edges of the wire-cut samples E-R and E-EB (50 N). This is highlighted by the line profiles of the DFI signal, see Fig. 5b), taken across the sample along the white line shown exemplary for SC-EB (50 N) and averaged between the dotted lines. The SCZ in SC-R is clearly visible as a reduction in DFI towards the edges at y=±5 mm, where E-R does not show a significant change in DFI from the average. However, embossing suppresses this distinction between shear cut and wire-cut samples, as there is no discernible difference between E-EB (50 N) and SC-EB (50 N) apart from a slightly higher DFI signal at y = 5 mm. The slightly higher DFI signal of SC-R, between y=±4 mm, can be attributed to the magnetic flux being displaced to the centre due to the locally reduced permeability at the edges, leading to a higher state of magnetization and, thus, a higher DFI signal. The slight difference between E-EB (50 N) and SC-EB (50 N) visible in SST measurements is not discernible in the DFI signal.

The specific magnetic losses P_S for the above-introduced specimen are compared to assess iron loss for embossed specimens and potential interactions with shear cut edges. Fig. 4c) visualises the specific magnetic losses P_s at f = 50 Hz. EB samples show higher losses for all studied polarisations. SC samples show slightly higher losses than the reference samples E. A higher F_{EB} increases the specific losses. The losses are especially pronounced for the SC-EB samples with F_{EB} = 100 N, where P_s exceeds 20 W/kg at 1.8 T For different frequencies of f = 50 Hz, 700 Hz, and 1000 Hz the specific magnetic losses at a polarisation level of 1.0 T are depicted in Fig. 6. E-EB is normalised to E-R, the other datasets are normalised to the SC-R reference. At f = 50 Hz, the embossed samples

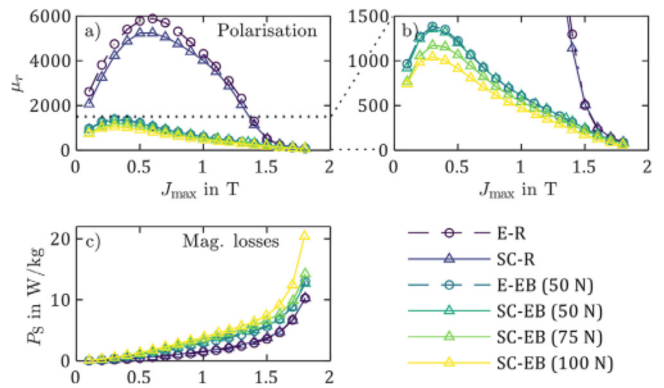

Fig. 4. a) Polarisation curves with f = 50 Hz for shear cut (SC) and wire-cut (E) samples with embossed (EB) and not-embossed (R) configurations for different F_{EB}; b) magnified view of a); c) specific magnetic losses P_S for the samples shown in a).

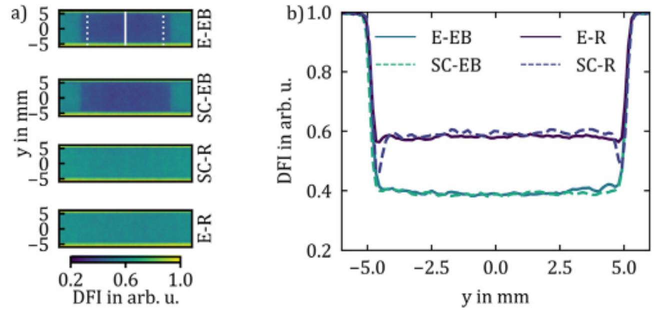

Fig. 5. a) DFI maps for shear cut (SC) and wire-cut (E) samples with embossed (EB) and not-embossed (R) configurations at 1000 A/m with F_{EB} = 50 N; b) DFI signal profiles taken from the white lines, depicted in a).

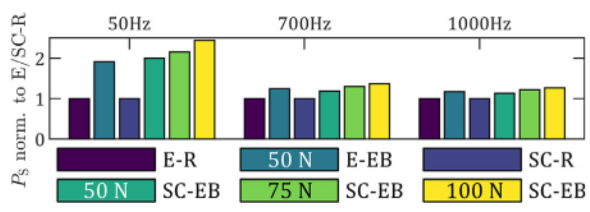

Fig. 6. Specific magnetic losses for f = 50 Hz, 700 Hz, 1000 Hz; E-EB is normalised to E-R, the other datasets are normalised to SC-R.

Please cite this article as: P. Stöcks-Morgan et al., Towards large-scale production of improved magnetic flux guidance structures in non-grain-oriented electrical steel, CIRP Annals - Manufacturing Technology (2025), https://doi.org/10.1016/j.cirp.2025.03.021

with F_{EB} = 100 N exhibit specific magnetic losses ∼2.5 times higher than the reference. However, as the magnetization frequency increases, the normalised specific magnetic losses decrease for embossed samples. The frequency-dependent behaviour of magnetic losses can explain this trend. While structural defects caused by cutting and embossing contribute significantly to losses at lower frequencies, their relative impact diminishes at higher frequencies where eddy current losses dominate.

3.3. Process sequencing: shear cutting and embossing

To study the influences of different process sequencing, samples with identical F_{EB} per area were produced on a universal testing machine. A fixed F_{EB} = 50 N is used. The measured DFI data, depicted in Fig. 7, shows no appreciable difference between the sequence of manufacturing steps. First shear cutting and then embossing (SC-EB), see Fig. 7a), as well as first embossing and then shear cutting (EB-SC), see Fig. 7b), provide the same flux suppression. This is exemplified in the practically identical DFI maps for the two manufacturing sequences at 1000 A/m. In Fig. 7c), the change of the mean DFI signal in the embossed area, dependent on the magnetic field, is shown in turquoise and yellow, respectively. The quotient of both curves (purple) underlines that there is almost no difference between the varied sequencing. The rise in DFI signal in the embossed areas is also nearly identical. The EB-SC sample shows a slightly higher flux suppression, as shown by the ratio of the two signals. This effect is attributed to general variations in the material. There is also no effect at the sample edges, where one would expect the largest difference: Fig. 7d) shows no influences of the SCZ when superimposed with embossing, independent of the process sequencing. From a magnetic property point of view, the manufacturing sequence is not important, but from a mechanical point of view, the sequence of first embossing and then shear cutting will result in better tolerances. Hence, it is the preferred sequence.

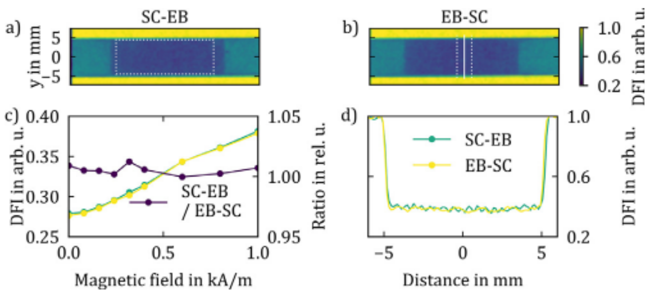

Fig. 7. Comparison of the DFI maps for a) shear cutting followed by embossing and b) embossing followed by shear cutting at 1000 A/m; c) the trend of the DFI signal dependent on the magnetic field and the ratio between the two processes is shown. Values form area marked in a). In d), the edge profile of the two specimens is presented, as marked in b).

3.4. Industrial outlook

The embossing was reproduced on the same material with coating. Laser optical analysis shows limited damage (max. 17 µm) of the coating around the embossed pyramids. We predict that no areas with damaged insulation will come into contact. An indent pyramid base width of around 130 µm (F_{EB} = 50 N) was measured. The shifted embossing pattern (cf. Fig. 2c) results in a shifted stacking pattern. Therefore, it can be assumed that no damaged insulation area would contact the similar affected area on the next sheet when stacked; hence, the approach is transferrable to industrially relevant coated sheets.

The process times for the different embossing methods are depicted in Fig 8a), showing fast manufacturability for simultaneously produced flux barriers on eccentric presses. The required press forces for shear cutting the motor geometry (shown in Fig 1a), compared to the additional force required for embossing, depicted in Fig 8b), show that embossing requires around 30–60% additional press force.

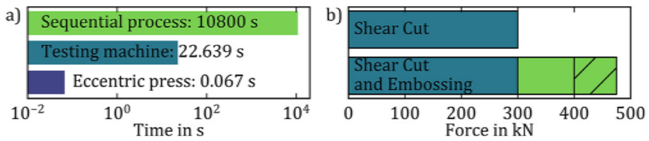

Fig. 8. a) Comparison of the required embossing times with different processes considering a 30×30 mm^2 area with 3600 embossing points on each side; b) required force for shear cutting (turquoise) and embossing (green) for the rotor geometry from Fig 1a). The hatched area shows the variation in embossing force dependent on the embossing geometry.

4. Conclusions

This paper presents the necessary investigations for transferring residual stress-based magnetic flux barriers in rotating electrical machines to large-scale production. Embossed flux barriers were manufactured on an industry-grade eccentric press for the first time: nGI data showed that embossed patterns of similar homogeneity could be obtained compared to a testing machine. The global SST characterisation of the samples showed a forced-dependent permeability reduction due to embossing. nGI measurements could prove that the effect originates from the embossed regions. The specific magnetic losses increased for embossed specimens; however, embossing is to be applied in small areas compared to the total rotor area. Superimposing embossed flux barriers with shear-cut edges showed that, while visible without embossing, the SCZ influence vanishes when superimposed with embossing. Process sequencing remains flexible since no magnetically preferable order of shear cutting and embossing could be found. Embossing damages coating around the indents, yet a short circuit can be avoided if a shifted embossing pattern is used.

With the manufacturability, process integrability and general function of embossed flux barriers being shown, the approach can finally be transferred to a series-produced motor geometry.

Declaration of competing interest

The authors declare that they have no known competing financial interests or personal relationships that could have appeared to influence the work reported in this paper.

CRediT authorship contribution statement

Phillip Stöcks-Morgan: Writing – review & editing, Writing – original draft, Visualization, Validation, Resources, Methodology, Investigation, Formal analysis, Data curation, Conceptualization. **Tobias Neuwirth:** Writing – original draft, Visualization, Software, Methodology, Investigation, Formal analysis, Data curation, Conceptualization. **Achref Douiri:** Writing – original draft, Investigation, Formal analysis, Data curation. **Simon R. Sebold:** Writing – original draft, Software, Methodology, Formal analysis, Visualization. **Anders Kaestner:** Resources, Investigation, Data curation. **Christoph Hartmann:** Writing – review & editing, Supervision, Resources, Project administration. **Nora Leuning:** Writing – review & editing, Writing – original draft, Supervision, Funding acquisition. **Michael Schulz:** Writing – review & editing, Supervision, Resources, Funding acquisition. **Wolfram Volk:** Writing – review & editing, Supervision, Resources, Funding acquisition.

Acknowledgments

This work is funded by the Deutsche Forschungsgemeinschaft (DFG, German Research Foundation) – 532773068. Additional support was received from PSI Center for Neutron and Muon Sciences in Villingen, Switzerland.

The authors would like to thank Ines Gilch for the embossing tool design, Lukas Martinitz for the geometrical analysis, Corinna Sutter for the metallographic analysis, and Paul Tkacz for assisting during the Neutron measurements.

Please cite this article as: P. Stöcks-Morgan et al., Towards large-scale production of improved magnetic flux guidance structures in non-grain-oriented electrical steel, CIRP Annals - Manufacturing Technology (2025), https://doi.org/10.1016/j.cirp.2025.03.021

References

[1] Waide P, Brunner CU (2011) Energy-efficiency policy opportunities for electric motor-driven systems. *International Energy Agency (IEA) working paper* 1:33–40 www.iea.org/publications/freepublications/publication/EE_for_ElectricSystems.pdf.

[2] Pyrhönen J, Jokinen T, Hrabovcová V (2013) *Design of Rotating Electrical Machines*, Wiley, . https://doi.org/10.1002/9781118701591.

[3] Gilch I, Neuwirth T, Schauerte B, Leuning N, Sebold S, Hameyer K, Schulz M, Volk W (2021) *Impact of residual stress evoked by pyramidal embossing on the magnetic material properties of non-oriented electrical steel. In Archive of Applied Mechanics*, 91, Springer Science and Business Media LLC. 3513–3526. https://doi.org/10.1007/s00419-021-01912-6..

[4] Ionel DM, Popescu M, Dellinger SJ, Miller TJE, Heideman RJ, McGilp MI (2006) *On the variation with flux and frequency of the core loss coefficients in electrical machines*, *In IEEE Transactions on Industry Applications*, 42, Institute of Electrical and Electronics Engineers (IEEE). 658–667. https://doi.org/10.1109/tia.2006.872941..

[5] Silveyra M, Ferrara E, Huber DL, Monson TC, et al. (2018) Soft magnetic materials for a sustainable and electrified world. *Science* 362:eaao0195. https://doi.org/10.1126/science.aa0195.

[6] Krings A, Boglietti A, Cavagnino A, Sprague S (2017) Soft magnetic material status and trends in electric machines. *IEEE Transactions on Industrial Electronics* 64 (3):2405–2414. https://doi.org/10.1109/tie.2016.2613844. VolIssueInstitute of Electrical and Electronics Engineers (IEEE).

[7] Kestens L, Jacobs S (2008) *Texture control during the manufacturing of nonoriented electrical steels*, *Texture, Stress, and Microstructure*, 2008, Hindawi Limited. 1–9. https://doi.org/10.1155/2008/173083..

[8] Denkena B, Biermann D (2014) *Cutting edge geometries*, *CIRP Annals*, 63, Elsevier BV. 631–653. https://doi.org/10.1016/j.cirp.2014.05.009..

[9] Schoppa A, Schneider J, Roth J-O (2000) Influence of the cutting process on the magnetic properties of non-oriented electrical steels. *J Magn Magn Mater* Vols. 215−216:100–102. https://doi.org/10.1016/s0304-8853(00)00077-9.

[10] Weiss HA, Leuning N, Steentjes S, Hameyer K, Andorfer T, Jenner S, Volk W (2017) Influence of shear cutting parameters on the electromagnetic properties of non-oriented electrical steel sheets. *J Magn Magn Mater* 421:250–259. https://doi.org/10.1016/j.jmmm.2016.08.002.

[11] Moses AJ, Derebasi N, Loisos G, Schoppa A (2000) Aspects of the cut-edge effect stress on the power loss and flux density distribution in electrical steel sheets. *J Magn Magn Mater* Vols. 215−216:690–692. https://doi.org/10.1016/s0304-8853(00)00260-2.

[12] Cullity BD, Graham CD (2009) *Introduction to Magnetic Materials*, 2nd IEEE Press: NJ, USA.

[13] Gilch I, Hartmann C, Grünhag B, Volk W, Schauerte B, Leuning N, Hameyer K (2023) Residual stresses and magnetic material properties of embossed and cut magnetic flux barriers in non-oriented electrical steel under tensile load. *2023 13th International Electric Drives Production Conference (EDPC) (pp. 1−8). 2023 13th International Electric Drives Production Conference (EDPC)*, IEEE, ; 2023. https://doi.org/10.1109/edpc60603.2023.10372160.

[14] Neuwirth T, Backs A, Gustschin A, Vogt S, Pfeiffer F, Böni P, Schulz M (2020) A high visibility Talbot-Lau neutron grating interferometer to investigate stress-induced magnetic degradation in electrical steel. *Scientific Reports (Vol. 10, Issue 1)*, Springer Science and Business Media LLC, ; 2020. https://doi.org/10.1038/s41598-020-58504-7.

[15] Strobl M (2014) General solution for quantitative dark-field contrast imaging with grating interferometers. *Scientific Reports (Vol. 4, Issue 1)*, Springer Science and Business Media LLC, ; 2014. https://doi.org/10.1038/srep07243.

[16] Pfeiffer F, Grünzweig C, Bunk O, Frei G, Lehmann E, David C (2006) Neutron phase imaging and tomography. In physical review letters (Vol. 96, Issue 21). *American Physical Society (APS)* . https://doi.org/10.1103/physrevlett.96.215505.

[17] Kaestner AP, Hartmann S, Kühne G, Frei G, Grünzweig C, Josic L, Schmid F, Lehmann EH (2011) The ICON beamline − A facility for cold neutron imaging at SINQ. *Nuclear Instruments and Methods in Physics Research Section A: Accelerators, Spectrometers, Detectors and Associated Equipment (Vol. 659, Issue 1, pp. 387−393)*, Elsevier BV, ; 2011. https://doi.org/10.1016/j.nima.2011.08.022.